JGR

RESEARCH ARTICLE

Key Points:
- Colocated ring laser and STS2 to estimate Rayleigh and Love wave energy in microseism
- More Love wave energy in secondary microseism than Rayleigh wave energy
- Seasonal variations in Rayleigh-to-Love wave energy ratio

Seasonal variations in the Rayleigh-to-Love wave ratio in the secondary microseism from colocated ring laser and seismograph

Toshiro Tanimoto[1], Céline Hadziioannou[2], Heiner Igel[2], Joachim Wassermann[2], Ulrich Schreiber[3], André Gebauer[3], and Bryant Chow[2]

[1]Department of Earth Science and Earth Research Institute, University of California, Santa Barbara, California, USA, [2]Department of Earth and Environmental Sciences, Ludwig-Maximilians-University, Munich, Germany, [3]Forschungseinrichtung Satellitengeodaesie, Technische Universitaet Muenchen, Koetzting, Germany

Abstract Monthly variations in the ratio of Rayleigh-to-Love waves in the secondary microseism are obtained from a colocated ring laser and an STS-2 seismograph at Wettzell, Germany. Two main conclusions are derived for the Rayleigh-to-Love wave kinetic energy ratios in the secondary microseism; first, the energy ratio is in the range 0.8–0.9 ($<$1.0) throughout a year except for June and July. It means that Love wave energy is larger than Rayleigh wave energy most of the year by about 10–20%. Second, this ratio suddenly increases to 1.0–1.2 in June and July, indicating a larger fraction of Rayleigh wave energy. This change suggests that the locations and behaviors of excitation sources are different in these months.

1. Introduction

It has generally been assumed that there is more Rayleigh wave energy than Love wave energy in seismic noise within the microseismic frequency band (0.05–0.4 Hz). This is because the mechanism for exciting Rayleigh waves by ocean waves was established by *Longuet-Higgins* [1950], and it naturally explained an important feature of double-frequency bands in the microseisms, i.e., the primary and the secondary microseisms. On the other hand, the mechanism of exciting Love waves has never been clear. With the development of dense seismic arrays of broadband stations, however, it is becoming clear that there is surprisingly a large fraction of Love waves in the microseisms [e.g., *Nishida et al.*, 2008]. This paper lends support to these results and points out a new feature in the seasonal variation that is contained in the energy ratio between Rayleigh waves and Love waves.

Our basic motivation for this study was that there are surprisingly few data that constrain the energy partition between Rayleigh waves and Love waves in the microseisms. This applies to both the primary microseism (about 0.05–0.07 Hz) and the secondary microseism (about 0.10–0.40 Hz). Answering this question has not been easy because source areas are not well localized [e.g., *Chevrot et al.*, 2007] and seismic arrays that are needed to understand the sources have been scarce until recently [e.g., *Friedrich et al.*, 1998].

In one of few contributions to this problem, *Nishida et al.* [2008] estimated the ratio of Love waves to Rayleigh waves using an array of tilt meters in Japan. Since phase velocities of Rayleigh and Love waves are different, separation of these two types of waves is possible by an array study. Their conclusion was that there was more Love wave energy than Rayleigh wave energy below 0.1 Hz, but it changed above 0.1 Hz and Love wave energy became about 50% of Rayleigh wave energy. Similar studies have been conducted in other regions recently that take advantage of a number of seismic arrays, and we expect to see more results in this line of work in the near future [e.g., *Riahi et al.*, 2013; *Juretzek et al.*, 2015].

In this study, we take a different approach; we use a unique set of instruments at Wettzell (WET), Germany, where an STS-2 seismograph and a ring laser [*Schreiber et al.*, 2009; *Schreiber and Wells*, 2013] are colocated. We estimate the amount of Rayleigh waves from the vertical-component seismograph (STS-2) and the amount of Love waves from the ring laser. The ring laser records the rotation in the medium, and the records are dominated by SH-type waves, thereby allowing us to measure the amount of Love waves.

We already reported our basic method and preliminary results [*Tanimoto et al.*, 2015]. Since then we have extended our analysis to temporal changes in the Rayleigh-to-Love wave ratios for the secondary microseism. In this study, we also correct for the minimum resolution problem (section 3.2) that was not included in the
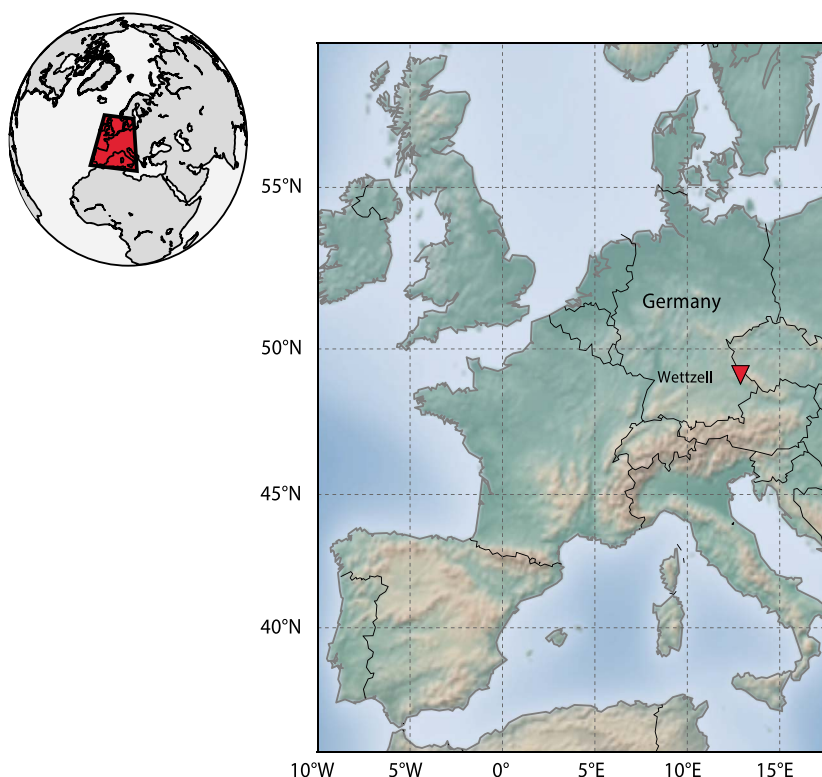
Figure 1. Station WET (Wettzell) is indicated by the red mark, close to the German-Czech border.

previous study. Because of the lack of this correction, our previous work led to some overestimates for the amount of Love waves. After this baseline correction, we find that the ratio of Love wave kinetic energy to Rayleigh wave energy is about 0.8–0.9 (<1.0) except for June and July. In these two months, this ratio increases to about 1.0–1.2. These two points are the main conclusions of this study.

We present the general characteristics of data at WET in section 2, our approach in section 3, the main results in section 4, and some discussions in section 5.

2. Data at Wettzell

In this study, we use a three-component seismograph (STS-2) and a ring laser at WET. For details on ring laser instruments, we refer the reader to *Schreiber and Wells* [2013]. The ring laser at WET measures the vertical (z) component of rotation rate $.\omega_z = (1/2)(\nabla \times \mathbf{v})$ where the dot denotes time derivative and $\mathbf{v}$ denotes ground velocity. There is a small possibility that tilt can contaminate the data, thus signals related to P-SV-type seismic waves (mostly Rayleigh waves) may get mixed in, but *Pham et al.* [2009] showed that the effects of tilt are negligible even for large earthquakes. We also examined this point in *Tanimoto et al.* [2015] and showed that the contribution from tilt is quite small (less than 0.1%) for seismic noise. Therefore, dynamically induced tilt, generated by seismic signals, does not seem to cause any serious contamination in the rotation measurement. There have been some reports of seasonally changing tilt due to thermoelastic effects [e.g., *Prawirodirdjo et al.*, 2006; *Ben-Zion and Allam*, 2013] whose magnitudes are large (~0.1 µrad). But their main frequency bands (~1 day) are 3 orders of magnitude lower than that of microseisms (0.05–0.40 Hz). Because of this difference in frequencies, these tilts are not relevant to seasonal variations in our results. In practice, the ring laser data in the frequency range of our analysis may be considered to be free from tilt contamination.

We rely on the vertical-component seismograph to estimate the amount of Rayleigh waves, but we also examine two horizontal components. Since both Rayleigh waves and Love waves are present in horizontal-component seismograms, it is hard to obtain clean information for each type of wave separately. But the comparison between the ring laser data and the horizontal seismograms provides some constraints. For example, our choice for the frequency range of this study was from 0.13 Hz to 0.30 Hz; this was influenced by comparison between
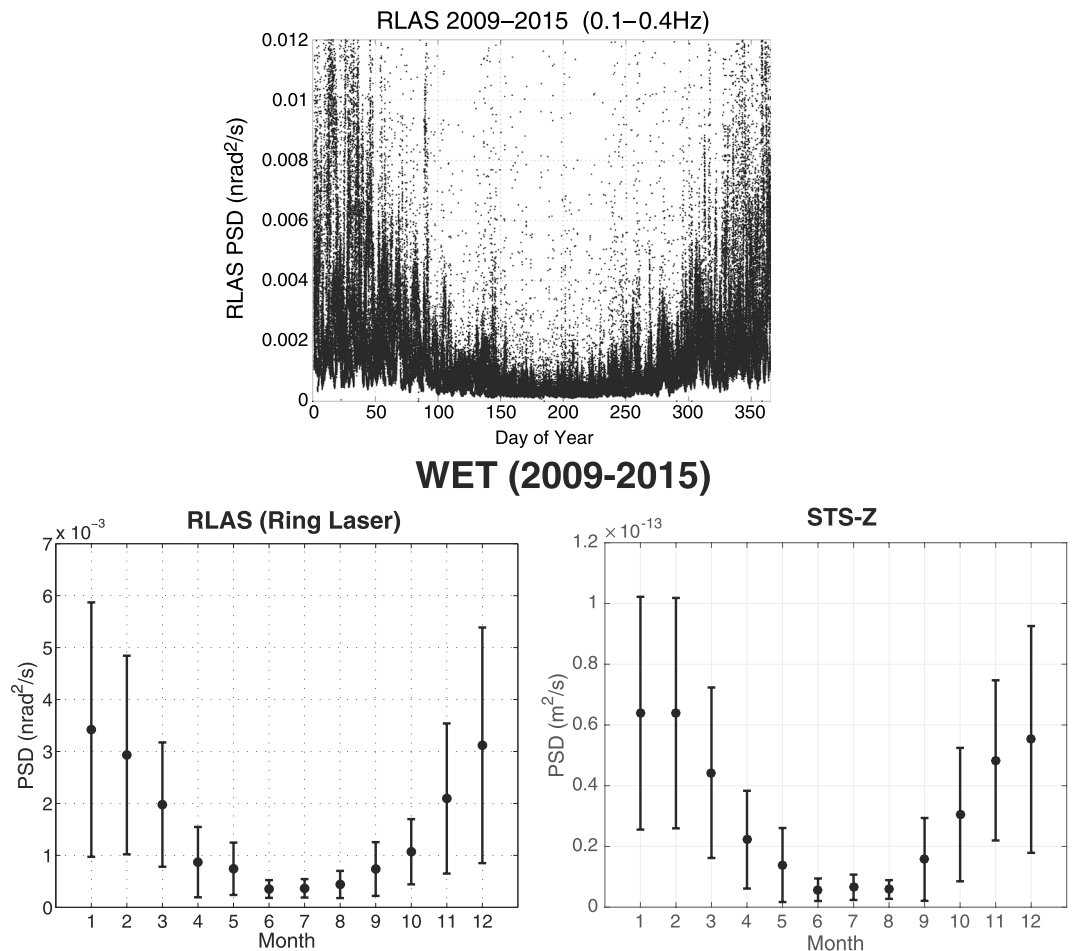
Figure 2. (a) Power spectral density (PSD) of rotation rate (0.1–0.4 Hz), recorded by the ring laser at Wettzell. Each point was computed from a 15 min long time series. Unit is nanoradians²/second. Data from 2009 to 2015 are folded onto 1 year using the Julian days. (b, left) Monthly averages of the ring laser data; the mean and one sigma standard deviation of the power spectral density (for frequencies 0.10–0.40 Hz) are shown. The abscissa is month in number. (b, right) Monthly averages of the vertical-component seismic data under the same conditions with ring laser data.

ring laser data and horizontal-component seismograms as ring laser-derived transverse accelerations (pure Love waves) and the horizontal-component accelerations (containing both Rayleigh and Love waves) cannot be different very much. We found large deviations for frequencies 0.10–0.12 Hz, for example, that were clearly anomalous. We thus chose the minimum frequency of our analysis at 0.13 Hz.

We analyzed the ring laser data at WET from 2009 to 2015. Figure 1 shows the location of Wettzell, in the Bavarian forest close to the German-Czech border. The ring laser provides time series of rotation rate (unit radian/second), and we used data that had 20 samples per second. Over this 6 year span, we computed the power spectral density (PSD) for every 15 min (Figure 2a). Each dot in Figure 2a shows an averaged PSD value between 0.1 and 0.4 Hz. PSD was computed by $|F(\omega)|^2/T$ where $F(\omega)$ is the Fourier spectra at an angular frequency ω and T is the length of time series (15 min). To be more precise, we applied the Hanning window to time domain signals, computed PSD using the above formula, and multiplied the correction factor 8/3 which compensates the reduction of power caused by the Hanning window [e.g., *Osaki*, 1976].

These PSD data are folded onto 1 year interval using the Julian days in Figure 2a. There are points above the maximum value in this figure, most of which were caused by earthquakes. As our goal is to study seismic noise, this study will focus on this small-amplitude range in Figure 2a. However, even in the data shown in Figure 2a, there may be some effects from earthquakes that are buried in the scatter of points. We remove these effects by using two earthquake catalogs.
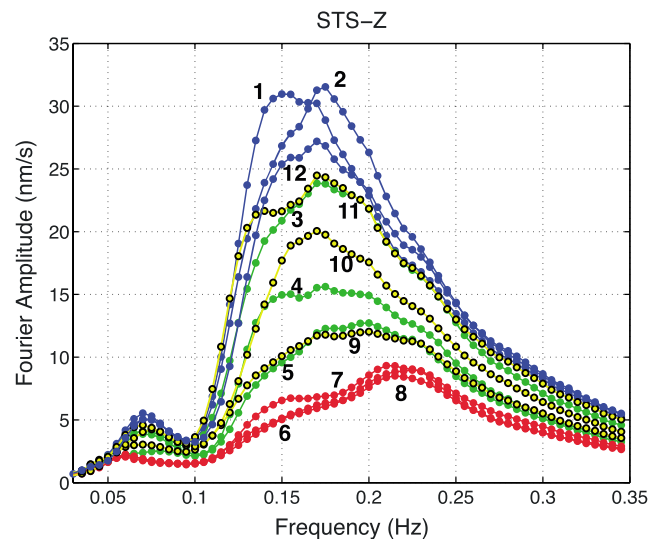
Figure 3. Monthly averages of Fourier spectral amplitude (normalized by the length of time series) for vertical-component seismograms after removal of earthquake effects. The numbers are used to denote months. For example, 1 is January, 2 is February, and so forth. Winter months (1, 2, 12) are in blue, summer months (6–8) are in red, spring months (3–5) are in green, and fall months (9–11) are in yellow with black circles.

Seasonal variations are obvious in the raw PSD data (Figure 2a). The monthly averages and error bars (one standard deviation) are shown in Figure 2b (left). The amplitudes in winter are about 8–10 times larger than the amplitudes in summer. In Figure 2b (right), we show the results of a similar analysis for the vertical-component seismograms. Since the ring laser data mostly contain Love wave energy and the vertical seismograph data mostly contain Rayleigh wave energy, we can directly confirm similar seasonal variations in both types of waves.

3. Approach

3.1. Monthly Averages

We first create the monthly-averaged Fourier amplitude curves both for the vertical-component seismograms and for the ring laser data. As the goal of this study is to estimate the amount of Love waves and Rayleigh waves in seismic noise, it is essential to make these data free of earthquake effects as much as possible.

We used two earthquake catalogs to remove earthquake effects. One is the Global Centroid Moment Tensor catalog (www.gcmt.org) which includes all events larger than $M = 5.5$ where M is the moment magnitude. This catalog also contains some smaller events than $M = 5.5$. In addition, we used a regional catalog from the European-Mediterranean Seismological Center (www.emsc-csem.org) in order to remove earthquake effects for events larger than $M = 4.5$ within the distance of 1000 km from WET.

Technically, we eliminate the portions in seismograms from our data set using the origin time of earthquakes and time length that we assign based on the size of earthquakes; specifically, for $M = 8$ or larger events anywhere in the world, we removed a whole day (24 h) after their origin time. For $M = 6$–8, we removed 12 h, and for events less than $M = 6$ ($M = 4.5$–6), we removed 6 h from the origin time.

Figure 3 shows the monthly-averaged spectral amplitudes for vertical-component data. We show the average of 15 min long Fourier amplitudes, not the power spectral density plotted in Figures 2a and 2b. A number by each line indicates a month. We use 1 for January, 2 for February, 3 for March, and so forth. The winter months (1, 2, 12) are shown in blue, and the summer months (6–8) are shown in red. The spring months (3–5) are in green, and the fall months (9–11) are in yellow (with black circles). One can see that these amplitudes are relatively stable both in summer and in winter but vary quickly in spring and fall months. In this plot, we can also see the peaks for the primary microseism at about 0.05–0.07 Hz and the predominant peaks for the secondary microseism between 0.1 and 0.3 Hz. The fact that we observe smooth monthly transitions in spectral amplitude indicates that earthquake effects were removed to a large extent.

Figure 4 shows the results of a similar analysis to the ring laser data. Uses of the numbers for months and the color scheme for each month are the same with Figure 3. The basic characteristics in monthly variations are the same with seismic data; the spectra in winter months (1, 2, 12) and those in summer months (6–8) are relatively stable. Amplitudes in spring months (3–5) and fall months (9–11) show quick transitions between the two end-member seasons, i.e., summer and winter.
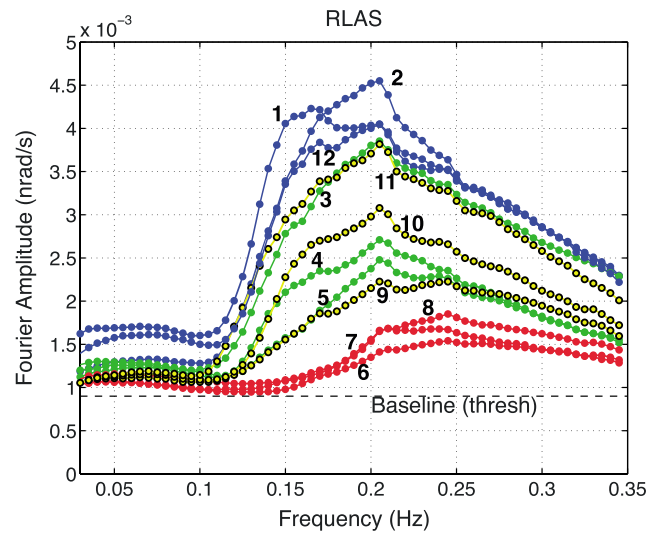
3.2. Baseline Correction

We have noted that the ring laser data hit the minimum resolution limit in the analysis (Figure 4). The dashed (horizontal) line in Figure 4 indicates this limit that we refer to as the baseline (or a threshold) hereafter.
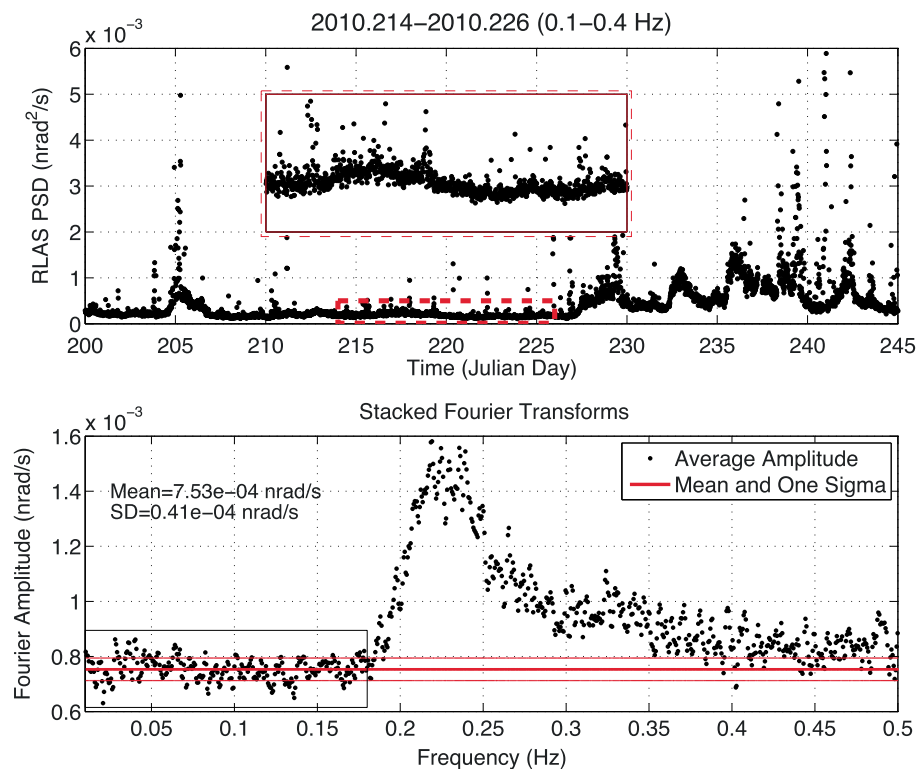
Figure 4. Same as Figure 3 except that this is for monthly averages of ring laser data. We find the minimum resolution limit in data (horizontal dash) which makes it difficult to study the primary microseism (0.05–0.07 Hz). This study focused on the secondary microseism for frequencies 0.13–0.30 Hz.

Existence of this minimum resolution is the reason that we cannot observe the peaks for the primary microseism (about 0.05–0.07 Hz, Figure 4). This lack of the peaks is in contrast with Figure 3 (from STS-2 vertical data).

In order to take care of this problem, we reanalyzed data and determined this baseline value. Figure 5 shows an example of such efforts where we focused on small-amplitude summer days in 2010 (Julian days from 214 to 226). For the time interval indicated by the red dash box in Figure 5 (top), we computed Fourier spectra for frequencies up to 0.5 Hz (Figure 5, bottom). These Fourier amplitudes show a clear peak associated with the secondary microseism (its maximum is about 0.22–0.24 Hz because this is summer), but amplitudes are flat below about 0.15 Hz. This feature

indicates that we have hit the minimum resolution for the ring laser. The mean and the standard deviation for amplitudes within a box (solid horizontal line in Figure 5, bottom) were computed using data below 0.1 Hz and led to an estimate of 0.753 ± 0.041 prad/s for the baseline value. The unit is picoradian per second. Further analyses from other time intervals led to an estimate of the baseline to be about 0.75–0.80 prad/s.

Figure 5. (top) Using the average PSDs in 2010 (Julian days from 214 to 226), shown by red box. (bottom) Fourier spectral amplitudes. Near constant amplitudes in the low-frequency range (up to about 0.15 Hz in Figure 5, bottom) are due to this minimum resolution limit. We determined this level and subtracted it from the ring laser data.
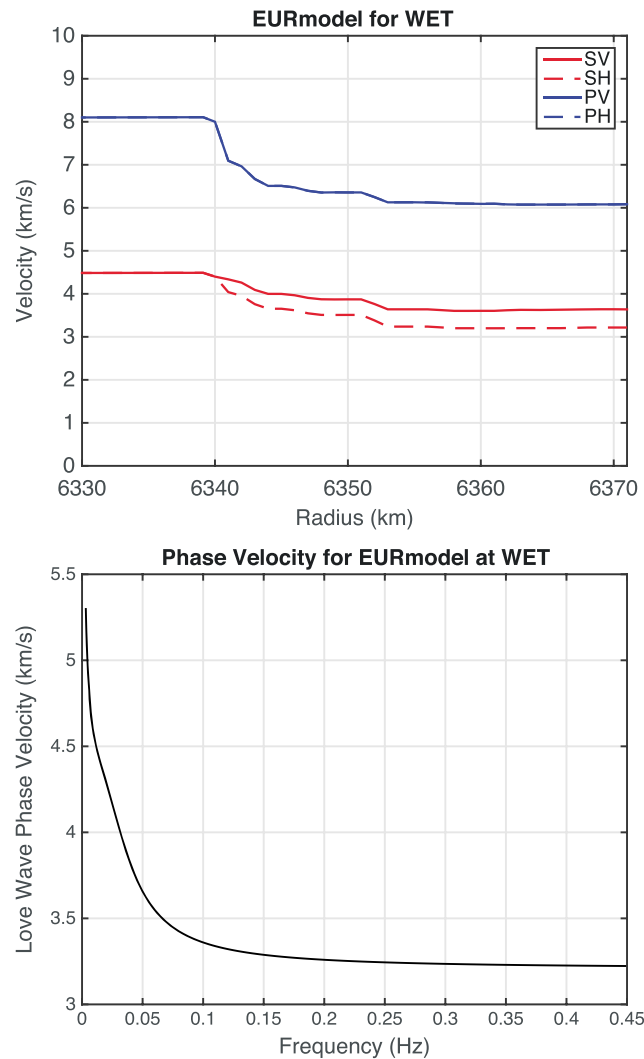
Figure 6. (top) *P* wave and *S* wave structure at WET from a model of European continent [*Fichtner et al.*, 2013]. The right edge is the Earth's surface (radius 6371 km) and PV, PH, SV, and SH velocities are shown. The abscissa is the radius from the center of the Earth. (bottom) Love wave fundamental-mode phase velocity computed for this model. The abscissa is frequency (Hz), and the ordinate is phase velocity (km/s).

Hereafter, for most figures in this paper, we show the results with the baseline value of 0.80 prad/s. The only exception is that the final monthly variation results will show the effects from an alternative choice of this value.

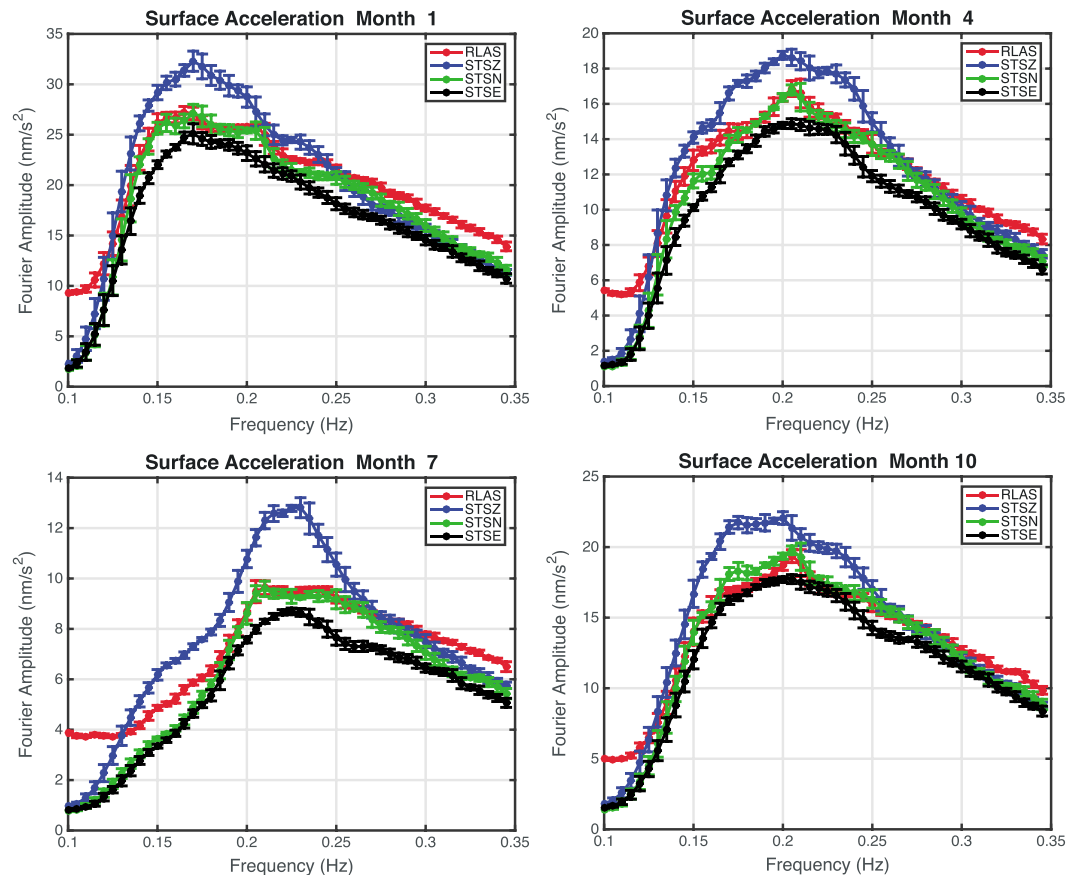We recalculated the Fourier amplitudes of the ring laser data using this baseline value (A_{BL}) by

$$U_{rot} = \sqrt{A_{RL}^2 - A_{BL}^2} \qquad (1)$$

where U_{rot} is a corrected rotation-rate amplitude and A_{RL} is an uncorrected Fourier amplitude shown in Figure 4. The underlying assumption is that seismic noise (our signal) is independent of the cause of this minimum resolution.

3.3. Conversion to Acceleration

Monthly spectral amplitudes from the seismometers (Figure 3) and the ring laser (Figure 4) are in different units and cannot be compared against each other directly. In order to compare using the same unit, we convert these data to acceleration. Since the vertical-component data from STS-2 are in ground velocity, a simple multiplication of angular frequency converts spectral amplitudes in Figure 3 to vertical accelerations.

For the rotation spectra, we need a few more steps of processing. We use the relation that a multiplication of 2*C* to the rotation spectra, where *C* is the local Love wave phase velocity, converts the rotation-rate data to surface transverse acceleration. This relationship was originally pointed out by *Pancha et al.* [2000] for two earthquakes and later used by *Igel et al.* [2005], *Igel et al.* [2007], *Ferreira and Igel* [2009], *Kurrle et al.* [2010], and *Hadziioannou et al.* [2012]. This processing assumes that Fourier amplitude spectra for the ring laser data consist of the fundamental-mode Love waves only. This assumption is only approximate as body waves and higher-mode surface waves have been identified in seismic noise; however, since the excitation sources for seismic noise are quite shallow, seismograms are dominated by fundamental-mode surface waves and thus we believe this assumption is justified to a large extent.

In order to apply this relation to rotation data, we need to know the local Love wave phase velocity at WET. In this study, we use an Earth model reported by *Fichtner et al.* [2013], derived for the European continent; we used its structure at WET and computed theoretical Love wave phase velocities for further analysis. Figure 6 shows the *P* wave and *S* wave velocity models at WET. It is an anisotropic (transversely isotropic) model, and Figure 6 shows PV, PH, SV, and SH velocities [e.g., *Takeuchi and Saito*, 1972]. Figure 6 (bottom) shows Love wave phase velocity for this model up to 0.45 Hz. Love wave phase velocity is about 3.2–3.3 km/s, but it has a uniformly decreasing trend with frequency in the frequency band of this study (0.1–0.4 Hz).

Figure 7. Transverse accelerations from ring laser are shown in red (pure SH signals). Vertical, NS, and EW accelerations are shown in blue, green, and black, respectively. Results for (top left) January (month 1), (top right) April (month 4), (bottom left) July (month 7), and (bottom right) October (month 10) are shown.

Figure 7 shows comparisons between surface accelerations for the months of January, April, July, and October. Each panel contains four curves. Red lines are surface transverse accelerations, obtained by multiplying $2C$ to the rotation spectra (after baseline correction of 0.8 prad/s). Blue lines are vertical accelerations obtained from vertical spectral amplitudes in Figure 3. Green lines and black lines are surface accelerations derived from the NS component and the EW component of seismic data.

Comparison between Figures 3 and 4 shows that the peak frequency in the rotation data (Figure 4) appears to be shifted toward higher frequency with respect to the peak in the seismic data (Figure 3). The peak locations match in Figure 7, because the multiplication by $2C$ moves the rotation peak toward lower frequencies. This overall match in peak frequencies seems to support that the adopted seismic model for WET is quite reasonable.

We also note in Figure 7 that amplitudes of transverse acceleration (red) are quite close to amplitudes of horizontal acceleration from the NS (green) and EW (black) components. Since the NS and EW components in seismic data should contain both Rayleigh waves and Love waves, they may differ to some extent but should have similar amplitudes. The fact that they are all close in these linear plots suggests that our two assumptions on the Earth model (Love wave phase velocity) and on the predominance of fundamental-mode Love waves are reasonable assumptions.

However, we see some discrepancies in the low/high frequency ends in Figure 7. In the low-frequency end of Figure 7, below about 0.12 Hz, we find large transverse acceleration (from rotational measurements) and much smaller horizontal accelerations (from the NS and EW seismographs). For example, transverse acceleration is 3–4 times larger than horizontal accelerations at 0.1 Hz at face value. This difference suggests inconsistency because transverse acceleration contains Love wave energy, while horizontal accelerations contain both Rayleigh wave
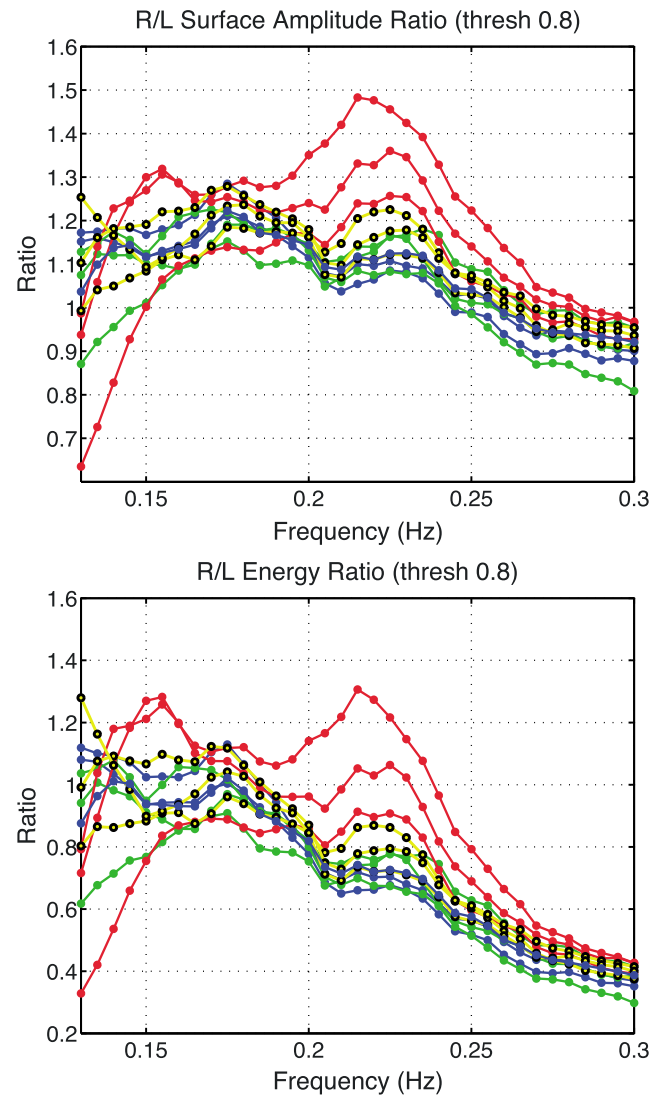
Figure 8. (top) Surface acceleration ratios between vertical acceleration and transverse acceleration. Each curve is for a month and is denoted by the same color scheme. These values are the ratios between the blue curves to the red curves in Figure 7. (bottom) The kinetic energy ratios between Rayleigh waves and Love waves. The same color scheme with Figure 3 is used for each month.

and Love wave energy. Considering the fact that the same Love wave energy is in both data, such a large transverse acceleration in comparison to horizontal accelerations seems problematic.
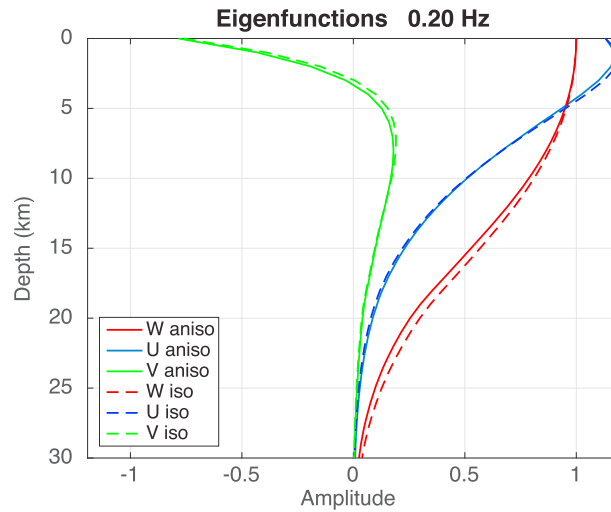
We believe this large deviation is most likely caused by the minimum resolution problem we discussed in section 3.2. For amplitudes near the baseline level (we used 0.8 prad/s), the correct signal level is hard to estimate from the use of equation (1) because there always exists some noise in addition to signals. When the signal level is much higher than the baseline value such as those in winter months, the correction by equation (1) works very well. In fact the corrected signals in winter are slightly smaller but are close to the original amplitudes (as in Figure 4). Amplitude behaviors in Figure 7 suggest that the transverse acceleration may contain some anomalous features below about 0.12 Hz and also above 0.30 Hz especially for summer months. Therefore, in the following analysis, we choose to analyze data in the frequency range 0.13–0.30 Hz only, where we do not see large deviations of transverse acceleration from two horizontal accelerations.

4. Rayleigh-to-Love Wave Ratio in the Secondary Microseism

4.1. Ratio of Surface Acceleration

We first measure the surface-amplitude ratios between vertical accelerations and transverse accelerations. This is simply done by taking the ratio of the blue curves to the red curves in Figure 7.

These ratios for each month are plotted in Figure 8 (top) using the same color scheme as in Figures 3 and 4. The abscissa is frequency and varies from 0.13 Hz to 0.30 Hz. The ordinate is the Rayleigh-to-Love ratio whose range is from 0.6 to 1.6. Most values exceed 1 in Figure 8, especially near the spectral peak range within 0.15–0.25 Hz. The values from summer (red) particularly stand out near their maximum frequency range about 0.22–0.23 Hz. On the average, the ratios between Rayleigh waves (vertical) to Love waves (transverse) are about 1.1–1.2. This ratio should be the same with ground velocity and displacement.

4.2. Ratio of Kinetic Energy

Next we convert these surface amplitudes to the kinetic energies of Rayleigh and Love waves. Our procedure proceeds as follows: we compute the eigenfrequencies and eigenfunctions of Rayleigh and Love waves for the seismic structure in Figure 6. Examples of eigenfunctions at 0.20 Hz are shown in Figure 9; the red solid line is the eigenfunction $W(z)$ of Love wave fundamental mode. The blue and green solid lines are the vertical $U(z)$ and horizontal eigenfunction $V(z)$ of Rayleigh wave fundamental mode. The depth coordinate z is from 0 (surface)

Figure 9. Examples of the eigenfunctions at 0.20 Hz used for computations of kinetic energy ratios. The seismic model in Figure 6 was used. Red is the eigenfunction (W) for Love waves (fundamental mode), and blue and green curves are the eigenfunctions (U and V) for Rayleigh waves (fundamental mode). Solid lines are for the original anisotropic model by *Fichtner et al.* [2013], while dashed lines are for the averaged isotropic model. Effects of anisotropy are not important for our results.

to infinity and is positive downward. These eigenfunctions are defined for displacement. In our definition, a Love wave eigenfunction $W(z)$ for an angular eigenfrequency ω and a wave number (k_x, k_y) is related to displacement as [e.g., *Takeuchi and Saito*, 1972]

$$u_x = -i\frac{k_y}{k}W(z)e^{i(\omega t - k_x x - k_y y)}$$
$$u_y = -i\frac{k_x}{k}W(z)e^{i(\omega t - k_x x - k_y y)}$$
$$u_z = 0$$

where the wave number vector defines the direction of propagation. A Rayleigh wave eigenfunction $U(z)$ and $V(z)$ are related to displacement by

$$u_x = -i\frac{k_x}{k}V(z)e^{i(\omega t - k_x x - k_y y)}$$
$$u_y = -i\frac{k_y}{k}V(z)e^{i(\omega t - k_x x - k_y y)}$$
$$u_z = U(z)e^{i(\omega t - k_x x - k_y y)}$$

Dashed lines in Figure 9 are the eigenfunctions of an isotropic medium when we averaged two P waves (PH and PV) and two S waves (SH and SV). Small differences between the anisotropic model and the isotropic model exist, but our results are mostly insensitive to the anisotropy of the medium.

Using the surface acceleration ratios in Figure 8 (top), we arrange the relative surface amplitudes of eigenfunctions between vertical and transverse components (U/W) and evaluate the kinetic energy integrals defined by

$$E_L = \omega^2 \int_0^\infty \rho W(z)^2 \, dz$$
$$E_R = \omega^2 \int_0^\infty \rho \left\{ U(z)^2 + V(z)^2 \right\} dz$$
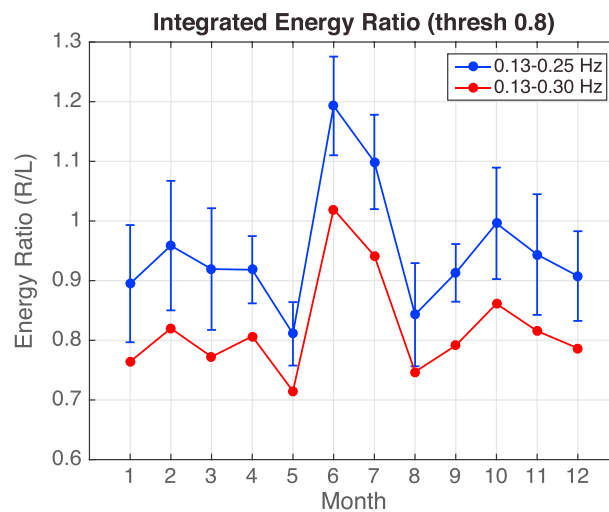
Figure 10. Monthly variations in the kinetic energy ratios between Rayleigh waves and Love waves (E_R/E_L). Blue is for the frequency range 0.13–0.25 Hz where the amplitude peaks are found. Red is for the frequency range 0.13–0.30 Hz. Both data show relatively stable values throughout a year except for June and July. Error bars are only shown for 0.13–0.25 Hz in order to reduce clutter, but they are similar for 0.13–0.30 Hz.

for Love waves and Rayleigh waves. Ratios of these kinetic energy integrals (E_R/E_L) are plotted in Figure 8 (bottom). These ratios become smaller than the surface acceleration ratios because Love wave energy penetrates slightly deeper than Rayleigh wave energy for the same frequency (Figure 9). The average of the kinetic energy ratios becomes slightly smaller than 1.0 (Figure 8, bottom).

The integrated kinetic energy ratios over two frequency bands are shown in Figure 10. The abscissa is month denoted by numbers from January (1) to December (12). The ordinate is the kinetic energy ratio. The blue curve shows the ratio for the frequency band from 0.13 to 0.25 Hz where we find the amplitude peaks of the secondary microseism. The red line shows the case when we extend the highest-frequency range from 0.25 Hz to 0.30 Hz. This case maintains the shape in monthly variations, but the whole curve is
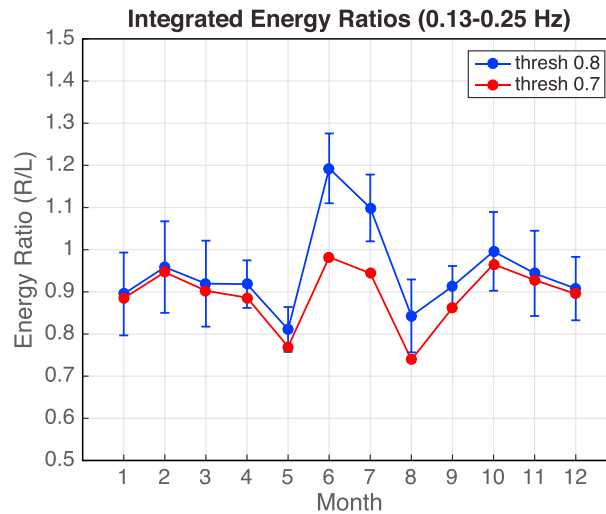
Figure 11. Effects of the baseline values (threshold) on the kinetic energy ratios. Two cases (0.7 and 0.8) are shown. Our preferred value for the baseline is 0.75–0.80 (prad/s). Higher ratios in June and July are affected by this choice but within our preferred values, the ratio shows a sudden increase. Error bars are only given for the blue curve, but they are quite similar for the red curve.

shifted to lower values because the ratios are small between 0.25 Hz and 0.30 Hz.

A characteristic feature in Figure 10 is the relatively constant ratio except for June and July. The blue curve (0.13–0.25 Hz) shows that the ratios are about 0.9 (0.8–1.0) most of the year except June and July. Therefore, except for these two months, there is approximately 10% more Love wave energy than Rayleigh wave energy. In the frequency band 0.13–0.30 Hz (red curve), the ratio is about 0.8, meaning Love wave energy is about 25% larger than Rayleigh wave energy. Therefore, this energy ratio depends on the frequency range, but Love wave energy is always slightly larger than Rayleigh wave energy.

The increase of ratios for June and July is about 20–30% in both frequency ranges. This feature seems to be relatively robust in our results.
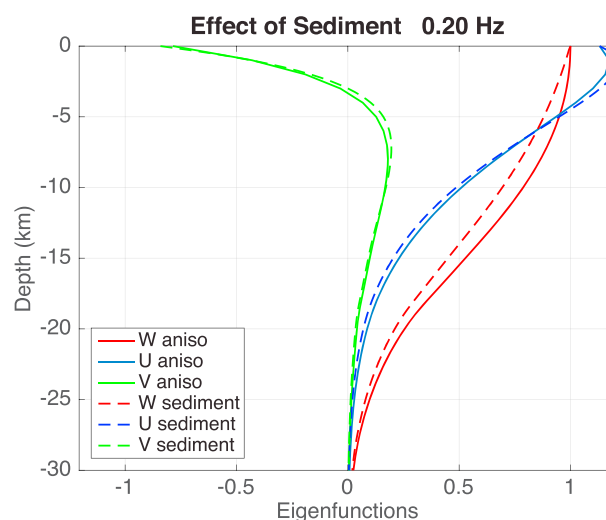
4.3. Effects of Baseline Values

As we discussed in section 3.2, the ring laser data have the minimum resolution limit and in our unit of Fourier amplitude, it is about 0.75–0.80 prad/s. Our results in Figures 8 and 10 were derived for the baseline (threshold) value of 0.8. Figure 11 compares the kinetic energy ratios for the baseline values of 0.7 and 0.8. We also included standard deviations for the results with 0.8. standard deviations for the baseline value of 0.7 (red) are about the same and are not plotted here to avoid clutter. Both curves are for the frequency range 0.13–0.25 Hz, and the blue curve is the same as the one in Figure 10.

Figure 11 shows that if we choose the baseline value of 0.7, the jump in the Rayleigh-to-Love wave ratio almost disappears. However, our best estimate of the baseline value is 0.75–0.80 (prad/s), and the baseline value is unlikely to be close to 0.70. For the baseline value of 0.75, the jump will be smaller than that for 0.80 but it is still about 20%. Thus, we believe that there is a jump in the kinetic energy ratio in June and July, which reaches about 20–30%.

Figure 12. Effects of a shallow low-velocity layer on the eigenfunctions. Solid lines are the same with Figure 9 (anisotropic case). Dashed lines are the eigenfunctions for a structure with a low-velocity sedimentary layer in the upper 250 m. P wave velocity is 2 km/s, S wave velocity is 1 km/s, and density is 2300 kg/m^3 in this layer.

There is a hint of small Rayleigh-to-Love wave ratio in May (5) and August (8) in Figures 10 and 11. This could be true, but the size of uncertainties weakens the significance of these features. We do not think that the lower ratios in May and August are robust features in our results.

5. Discussion and Conclusion

We have demonstrated that a colocated ring laser and a three-component seismometer (STS-2) at WET allowed us to separate Rayleigh waves and Love waves in the secondary microseism (0.13–0.30 Hz) and enabled us to estimate their kinetic

energy ratios. We found that the Rayleigh-to-Love wave energy ratio is smaller than 1 most of the year. However, this ratio depends on a chosen frequency band; in the high-amplitude range of secondary microseism (0.13–0.25 Hz), this ratio was about 0.9. This ratio means that there is approximately 10% more Love wave energy than Rayleigh wave energy. In a slightly wider frequency band, 0.13–0.30 Hz, this ratio became about 0.8, indicating that there was about 25% more Love wave energy. While our estimates contain some uncertainties, Love wave kinetic energy seems to be consistently larger than Rayleigh wave energy for the secondary microseism. These are relatively robust results, but they were derived based on some assumptions and limitations in data. We will discuss three points below: (5.1) implications of large Love wave energy, (5.2) limitations from the minimum resolution, and (5.3) a need for a local seismic structure.

5.1. Implications of Large Love Wave Energy

A large partition of Love wave energy with respect to Rayleigh wave energy poses a challenge to our understanding of the excitation and propagation of seismic energy in the secondary microseism. The Longuet-Higgins mechanism, the wave-wave interactions of ocean waves [*Longuet-Higgins*, 1950], is generally accepted to be the main mechanism of excitation but because it is equivalent to a vertical force, it only excites Rayleigh waves for a layered medium. Even in the real three-dimensional Earth, it cannot be an efficient excitation source for Love waves. One of the main arguments to explain a large amount of Love wave energy has been to invoke Rayleigh-to-Love wave conversion at the ocean-continent boundary. This structural effect should be important as the structural contrast at ocean-continent boundaries is generally sharp; on this point there have been some careful studies by using numerical simulations [e.g., *Gualtieri et al.*, 2015] and undoubtedly there will be more such studies to come.

The question raised by our results is whether such conversion processes alone can explain a larger fraction of Love waves than Rayleigh waves in the secondary microseism. The wavelengths of these seismic waves are typically 10–30 km (period 5–10 s) and thus are not necessarily short in comparison to typical size of crustal heterogeneity. Scattering effects cannot be ignored but their severity may not be as strong as it would lead to an equipartition of energy between Rayleigh and Love waves. Therefore, a large fraction of Love wave energy in our results seems to suggest that there must be processes of Love wave generation through the interactions of ocean waves with the solid Earth; such interactions can be quite large close to the coast as propagating ocean waves in shallow depths can exert horizontal forces on the solid Earth [e.g., *Saito*, 2010].

Ardhuin et al. [2015] presented an attractive hypothesis of explaining the hum [e.g., *Suda et al.*, 1998; *Kobayashi and Nishida*, 1998; *Tanimoto et al.*, 1998] and the microseisms by a unified mechanism, but their arguments mostly applied to Rayleigh waves only. Our results indicate that the situations may be not so simple, as there is a large fraction of Love waves in the microseism. A similar conundrum exists for the toroidal hum whose source has not been understood very well [e.g., *Kurrle and Widmer-Schnidrig*, 2008].

5.2. Limitations From the Minimum Resolution Limit

Monthly variations in the Rayleigh-to-Love wave energy ratio showed an increase in June and July by about 20–30%, regardless of the chosen frequency band. However, the size of this energy increase was dependent on the choice of the baseline value. Among the preferred range of this value, 0.75–0.80 prad/s, this jump varied between about 20 and 30%. This estimate cannot be improved unless the baseline value (minimum resolution value for rotation) will be reduced further.

The minimum resolution limit (baseline) was also the reason that we could not conduct similar analyses to the primary microseism (0.05–0.07 Hz). Monthly amplitudes in Figure 4 suggest that if this limit can be lowered by a factor of 5 through instrumental improvement, we can observe the primary microseism and conduct similar analyses on it. This may appear a formidable challenge, but there is a precedence for it; an improvement of the mirrors in the ring laser in 2009 led to a sudden improvement of the signal-to-noise ratio by approximately a factor of 10 [*Igel et al.*, 2011; *Hadziioannou et al.*, 2012] and removed the concerns for small signals in ring laser data [*Widmer-Schnidrig and Zürn*, 2009].

5.3. Need for Accurate Local Structure

In our analysis, we relied on an Earth model for WET in a model of the European continent [*Fichtner et al.*, 2013] because a regional model was not available. The quality of our results hinges on the phase velocity

for this model, as phase velocities are simply multiplied to the rotation-rate data in order to obtain transverse acceleration.

This Earth model was also used to compute the eigenfunctions of Rayleigh and Love waves for the kinetic energy estimates. This model does not have a sedimentary layer at top; however, if a low-velocity sedimentary layer existed at WET, it may affect our energy estimates. This is because we determine surface amplitudes of Love and Rayleigh waves from data and use them to infer the total energy of surface waves.

Figure 12 shows the effects of sedimentary layer on the eigenfunctions when we placed a sedimentary layer with a thickness of 250 m at the surface. This sedimentary layer had P wave velocity of 2 km/s and S wave velocity of 1 km/s. Below 250 m, the same structure with Figure 6 (top) was kept for the computation. The solid lines are the same eigenfunctions with those in Figure 9 (anisotropic version), and the dashed lines are the eigenfunctions for the modified structure with sediment. The eigenfunctions of Rayleigh waves (U and V) change, but their deviations are not systematic with depth. Deviations are positive for some depths but are negative for other depths. On the other hand, the eigenfunction of Love waves (W) becomes systematically smaller from the presence of a sedimentary layer, and this leads to a smaller estimate of Love wave energy. In this case, the Love wave energy becomes 5–6% smaller. Considering the uncertainties in our estimates for the energy ratios (~10%), this is a concern but is not sufficiently large to change our conclusions.

If the thickness of this sedimentary layer can become thicker, we may need to revise our estimate for the energy ratios. However, a report by Jena Geos Ingenieurbüro (personal communication, 1998) stated that the thickness is less than 10 m. Also from an independent H/V ratio measurements, a case for a thicker sedimentary layer is not likely at WET; our measurement for H/V for the secondary microseism at WET indicates a ratio of about 1/1.4, approximately 40% larger vertical amplitudes than horizontal amplitudes (in the Rayleigh wave particle motion in the secondary microseism). Such a vertically elongated Rayleigh wave particle motion indicates that the structure cannot have a thick sedimentary layer. In fact, this H/V ratio is fit quite well by the model of *Fichtner et al.* [2013] which does not have a sedimentary layer. Therefore, we believe our result of large Love wave energy is still supported for WET. In general, we have not found any inconsistency between this Earth model (Figure 6) and other local data so far. But our results can be made more reliable if we can derive a local seismic structure using regional data sets. The key is in clarifying seismic velocity structure near the surface. We intend to do so in the future.

References

Ardhuin, F., L. Gualtieri, and E. Stutzmann (2015), How ocean waves rock the Earth: Two mechanisms explain microseisms with periods 3 to 300 s, *Geophys. Res. Lett.*, *42*, 765–772, doi:10.1002/2014GL062782.

Ben-Zion, Y., and A. A. Allam (2013), Seasonal thermoelastic strain and postseismic effects in Parkfield borehole dilatometers, *Earth Planet. Sci. Lett.*, *379*, 120–126.

Chevrot, S., M. Sylvander, S. Benahmed, C. Ponsolles, J. M. Lefe'vre, and D. Paradis (2007), Source locations of secondary microseisms in western Europe: Evidence for both coastal and pelagic sources, *J. Geophys. Res.*, *112*, B11301, doi:10.1029/2007JB005059.

Ferreira, A., and I. Igel (2009), Rotational motions of seismic surface waves in a laterally heterogeneous Earth, *Bull. Seismol. Soc. Am.*, *99*(2B), 1429–1436.

Fichtner, A., J. Trampert, P. Cupillard, E. Saygin, T. Taymaz, Y. Capdeville, and A. Villasenor (2013), Multiscale full waveform inversion, *Geophys. J. Int.*, *194*, 534–556, doi:10.1093/gji/ggt118.

Friedrich, A., F. Kruger, and K. Klinge (1998), Ocean-generated microseismic noise located with the Grafenberg array, *J. Seismol.*, *2*, 47–64.

Gualtieri, L., E. Stutzmann, Y. Capdeville, V. Farra, A. Mangeney, and A. Morelli (2015), On the shaping factors of the secondary microseismic wavefield, *J. Geophys. Res. Solid Earth*, *120*, 6241–6262, doi:10.1002/2015JB012157.

Hadziioannou, C., P. Gaebler, U. Schreiber, J. Wassermann, and H. Igel (2012), Examining ambient noise using co-located measurements of rotational and translational motion, *J. Seismol.*, *16*, 787, doi:10.1007/s10950-012-9288-5.

Igel, H., U. Schreiber, A. Flaws, B. Schuberth, A. Velikoseltsev, and A. Cochard (2005), Rotational motions induced by the M8.1 Tokachi-oki earthquake, September 25, 2003, *Geophys. Res. Lett.*, *32*, L08309, doi:10.1029/2004GL022336.

Igel, H., A. Cochard, J. Wassermann, A. Flaws, U. Schreiber, A. Velikoseltsev, and N. Pham Dinh (2007), Broad-band observations of earthquake-induced rotational ground motions, *Geophys. J. Int.*, *168*(1), 182–196.

Igel, H., M.-F. Nader, D. Kurrle, A.-M. G. Ferreira, J. Wassermann, and K. U. Schreiber (2011), Observations of Earth's toroidal free oscillations with a rotation sensor: The 2011 magnitude 9.0 Tohoku-oki earthquake, *Geophys. Res. Lett.*, *38*, L21303, doi:10.1029/2011GL049045.

Juretzek, C., M. Perleth, and C. Hadziioannou (2015), Characteristics of Love and Rayleigh waves in ambient noise: Wavetype ratio, source location and seasonal behavior, Paper S41B-2759, AGU Fall Meeting.

Kobayashi, N., and K. Nishida (1998), Continuous excitation of planetary free oscillations by atmospheric disturbances, *Nature*, *395*, 357–360.

Kurrle, D., and R. Widmer-Schnidrig (2008), The horizontal hum of the Earth: A global background of spheroidal and toroidal modes, *Geophys. Res. Lett.*, *35*, L06304, doi:10.1029/2007GL033125.

Kurrle, D., H. Igel, A.-M. G. Ferreira, J. Wassermann, and U. Schreiber (2010), Can we estimate local Love wave dispersion properties from collocated amplitude measurements of translations and rotations? *Geophys. Res. Lett.*, *37*, L04307, doi:10.1029/2009GL042215.

Longuet-Higgins, M. (1950), A theory of the origin of microseisms, *Philos. Trans. R. Soc. London, Ser. A*, *243*(857), 1–35.

Nishida, K., H. Kawakatsu, Y. Fukao, and K. Obara (2008), Background Love and Rayleigh waves simultaneously generated at the Pacific Ocean floors, *Geophys. Res. Lett.*, *35*, L16307, doi:10.1029/2008GL034753.

Osaki, Y. (1976), *Introduction to Spectral Analysis for Seismic Ground Motion* [in Japanese], Kajima Co., Tokyo.

Pancha, A., T. H. Webb, G. E. Stedman, D. P. McLeod, and K. U. Schreiber (2000), Ring laser detection of rotations from teleseismic waves, *Geophys. Res. Lett.*, *27*(21), 3553–3556, doi:10.1029/2000GL011734.

Pham, N., H. Igel, J. Wassermann, M. Kaser, J. de La Puente, and U. Schreiber (2009), Observations and modeling of rotational signals in the P-coda: Constraints on crustal scattering, *Bull. Seismol. Soc. Am.*, *99*(2B), 1315–1332.

Prawirodirdjo, L., Y. Ben-Zion, and Y. Bock (2006), Observation and modeling of thermoelastic strain in Southern California Integrated GPS Network daily position time series, *J. Geophys. Res.*, *111*, B02408, doi:10.1029/2005JB003716.

Riahi, N., G. Bokelmann, P. Sala, and E. H. Saenger (2013), Time-lapse analysis of ambient surface wave anisotropy: A three-component array study above an underground gas storage, *J. Geophys. Res. Solid Earth*, *118*, 5399–5351, doi:10.1012/jgrb.50375.

Saito, T. (2010), Love-wave excitation due to the interaction between a propagating ocean wave and the sea-bottom topography, *Geophys. J. Int.*, *182*, 1515–1523, doi:10.1111/j.1365-246X.2010.04695.x.

Schreiber, U., and J.-P. Wells (2013), Invited review article: Large ring laser for rotation sensing, *Rev. Sci. Instrum.*, *84*, 041101, doi:10.1063/1.4798216.

Schreiber, U., J. N. Hautmann, A. Velikoseltsev, J. Wassermann, H. Igel, J. Otero, F. Vernon, and J.-. P. R. Wells (2009), Ring laser measurements of ground rotations for seismology, *Bull. Seismol. Soc. Am.*, *99*(2B), 1190–1198, doi:10.1785/0120080171.

Suda, N., K. Nawa, and Y. Fukao (1998), Earth's background free oscillations, *Science*, *279*, 2089–2091.

Takeuchi, H., and M. Saito (1972), Seismic surface waves, in *Methods in Computational Physics*, vol. 11, pp. 217–295 , Academic Press, New York.

Tanimoto, T., J. Um, K. Nishida, and N. Kobayashi (1998), Earth's continuous oscillations observed seismically quiet days, *Geophys. Res. Lett.*, *25*, 1553–1556, doi:10.1029/98GL01223.

Tanimoto, T., C. Hadziioannou, H. Igel, J. Wasserman, U. Schreiber, and A. Gebauer (2015), Estimate of Rayleigh-to-Love wave ratio in the secondary microseism by colocated ring laser and seismograph, *Geophys. Res. Lett.*, *42*, 2650–2655, doi:10.1002/2015GL063637.

Widmer-Schnidrig, R., and W. Zürn (2009), Perspectives for ring laser gyroscopes in low-frequency seismology, *Bull. Seismol. Soc. Am.*, *99*(2B), 1199.